ACS OMEGA

http://pubs.acs.org/journal/acsodf

Article

Tuning the Electrocatalytic Properties of Black and Gray Arsenene by Introducing Heteroatoms

Sengpajan Santisouk,[#] Phoxay Sengdala,[#] Xingxing Jiang, Xiong-Xiong Xue,* Ke-Qiu Chen, and Yexin Feng*

Cite This: *ACS Omega* 2021, 6, 13124−13133

Read Online

ACCESS | Metrics & More | Article Recommendations | Supporting Information

ABSTRACT: On the basis of density functional theory calculations, we explored the catalytic properties of various heteroatom-doped black and gray arsenene toward the oxygen reduction reaction (ORR), the oxygen evolution reaction (OER), and the hydrogen evolution reaction (HER). The calculation results show that pristine black (b-As) and gray arsenene (g-As) exhibit poor catalytic performance because of too weak intermediate adsorption. Heteroatom doping plays a key role in optimizing catalytic performance. Among the candidate dopants O, C, P, S, and Sb, O is the most promising one used in arsenene to improve the ORR and OER catalytic performance. Embedding O atoms could widely tune the binding strength of reactive intermediates and improve the catalytic activity. Single O-doped g-As^1_O can achieve efficient bifunctional activity for both the OER and the ORR with optimal potential gap. b-As^1_O and b-As^2_O exhibit the optimal OER and ORR catalytic performance, respectively. For the HER, double C-doped g-As^2_C could tune the adsorption of hydrogen to an optimal value and significantly enhance the catalytic performance. These findings indicate that arsenene could provide a new platform to explore high-efficiency electrocatalysts.

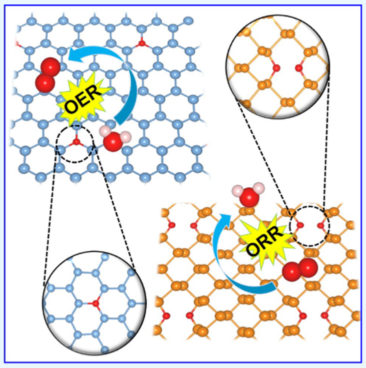

INTRODUCTION

The development of effective catalysts for the oxygen reduction reaction (ORR), the oxygen evolution reaction (OER), and the hydrogen evolution reaction (HER) are highly desirable for new clean energy technologies. Nowadays, various two-dimensional (2D) layered materials have been extensively explored as high-performance catalysts, including heteroatom-doped graphene for the ORR and OER,[1,2] black phosphorus (BP) for the OER,[3−5] MoS_2 and SnS_2 for the HER,[6,7] transition-metal-anchored C_2N for the HER and OER,[8] etc.[9,10]

Recently, elemental 2D layered arsenic (As) of the same group V element as P has attracted extensive attention due to its unique electronic and structural properties. Arsenic exists in two most widely studied allotropes: black arsenic and gray arsenic.[11−14] As a cousin of BP, black arsenic also possesses the orthorhombic puckered honeycomb structure.[11,12] Gray arsenic has the same hexagonal buckled geometry as blue phosphorus.[12] Some studies have verified that black arsenic shows anisotropic and thickness-dependent semiconductor characteristics.[15,16] Upon reducing the layer numbers to the monolayer, black arsenic exhibits the transformation of the direct−indirect band gap,[17] while gray arsenic exhibits the transformation from semimetals to semiconductors.[18] More importantly, black and gray arsenic monolayers (arsenene) have been predicted to possess high carrier mobility,[15,16,19] which will accelerate the electron transport of the electrocatalytic reaction. Black and gray arsenene also possess a relatively good environmental stability that is critical for catalytic durability.[16] On the basis of these distinct properties, arsenene has shown great potential for many emerging applications, including thermoelectric applications[20,21] and field-effect transistors.[16] In addition to the above applications, these excellent structural and electronic characteristics may also endow arsenene with potential catalytic application for the ORR, OER, and HER.

Pristine black and gray arsenene could also be chemically modified to exhibit superior structural and electronic properties. For example, Sturala et al. have predicted that through chemical modification of the surface, multilayer and monolayer arsenic materials can obtain large surface coverage and high luminescence.[22] Li et al. have suggested that by doping heteroatoms B, C, N, O, etc., gray arsenene can realize tunable electronic structures and magnetic properties, which indicates that doped gray arsenene will possess promising potential for applications in electronics and spintronics.[23] In addition, it was reported that O-dopant-modified black arsenene can act as an effective HER electrocatalyst with high catalytic activity.[24] Therefore, we believe that impurity doping could greatly tune the catalytic activities of black and gray arsenene. Although

Received: February 19, 2021
Accepted: May 4, 2021
Published: May 11, 2021

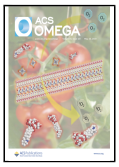

© 2021 The Authors. Published by American Chemical Society

https://doi.org/10.1021/acsomega.1c00908
ACS Omega 2021, 6, 13124−13133

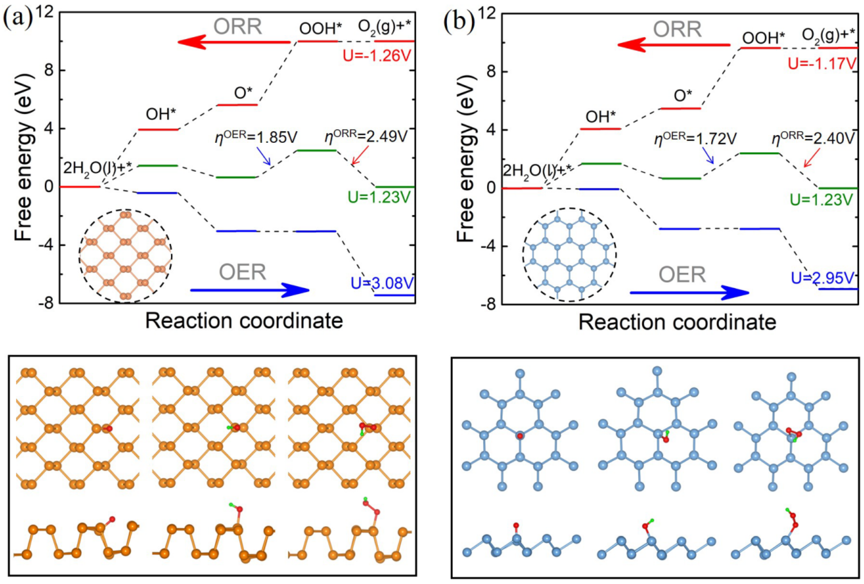

Figure 1. Free-energy diagrams for OER and ORR elementary steps on pristine (a) black and (b) gray arsenene at different electrode potentials *U*. The atomic structures (top and side views) of the adsorbed intermediates O*, OH*, and OOH* are also shown below each diagram.

great progress has been made in investigating the geometric structures and electronic properties of pristine and impurity-doped arsenene, experimental and theoretical research toward the ORR, OER, and HER of heteroatom-doped black and gray arsenene materials has never been reported.

In this work, based on density functional theory (DFT) calculations, the ORR, OER, and HER catalytic performances of heteroatom-doped black arsenene (b-As) and gray arsenene (g-As) have been studied. The results show that O atoms are more easily embedded into the arsenene lattice than other heteroatoms, especially for double O-atom doping. By calculating the overpotentials of the ORR/OER processes and the Gibbs free energy of H* adsorption for the HER, we find that pristine b-As and g-As exhibit poor catalytic activities. O and C dopants can effectively tune the absorption strength of intermediates and thus enhance catalytic activities. Single O-doped g-As_O^1 is best suited for the OER process, and optimal ORR activities could be realized on double O-doped b-As_O^2. The reaction free energies of H* could be optimized to the appropriate value on double C-doped g-As_C^2, indicating improved HER catalytic performance. The present findings could provide a useful guidance for developing multifunctional arsenene-based metal-free catalysts.

■ COMPUTATIONAL METHODS

First-principle calculations were performed within the framework of spin-polarized DFT, as implemented in the Vienna Ab Initio Simulation Package (VASP).[25,26] The projector augmented wave pseudopotential is used to describe nuclei−electron interactions,[27] while the electronic exchange−correlation corrections were described within the generalized gradient approximation, as parameterized by Perdew−Burke−Ernzerhof.[28] A cutoff energy of 500 eV was used within the plane wave basis set. To evaluate the catalytic performance, we constructed 4 × 4 × 1 b-As and 5 × 5 × 1 g-As supercells, as shown in Figure S1. The Brillouin zone was sampled using a 5 × 5 × 1 Monkhorst−Pack grid centered at the gamma (Γ) point. All atoms in the cell are fully optimized until the force acting on each atom is less than 0.02 eV $Å^{-1}$. A vacuum region of 15 Å is created in the slab model to neglect the interaction between adjacent models, and we employ the DFT-D3 scheme to describe the dispersion interaction between model surfaces and adsorbed intermediates.[29,30]

The formation energies E_f's of substitutional atoms (O, C, P, S, and Sb) in b-As and g-As lattices are calculated by[31,32]

$$E_f = E_{tot}(m) - E_{tot} - m\mu_X + m\mu_{As} \quad (1)$$

where $E_{tot}(m)$ and E_{tot} are the total energies of the heteroatom-doped and pristine b-As/g-As surface, respectively; μ_{As} is the chemical potential of As and is calculated from the bulk phase of As; μ_X is the chemical potential of the introduced *X* atoms (*X* = O, C, P, S, and Sb) and calculated as in O_2, graphene, bulk phase of BP, alpha-S, and Sb, respectively; and *m* is the number of substituted X atoms in the model.

According to the standard hydrogen electrode method, the four-electron ORR and OER reaction progress is investigated in an acidic environment.[33,34] The OER could occur along the following reaction paths:

$$H_2O(l) + * \rightarrow OH* + (H^+ + e^-) \quad (2)$$

$$OH* \rightarrow O* + (H^+ + e^-) \quad (3)$$

$$O* + H_2O(l) \rightarrow OOH* + (H^+ + e^-) \quad (4)$$

$$OOH* \rightarrow O_2(g) + * + (H^+ + e^-) \quad (5)$$

where * stands for the absorption site on the catalyst surface; (l) and (g) indicate the liquid and gas phases, respectively; O*, OH*, and OOH* represent the adsorbed intermediates. The ORR reaction is the reverse process of the OER listed above from eqs 2−5.

The ORR and OER overpotentials (η's) can be obtained by calculating the Gibbs free energy ΔG for each reactive step of eqs 2−5. ΔG is defined by the following equation:

$$\Delta G = \Delta E + \Delta ZPE - T\Delta S + \Delta G_U + \Delta G_{PH} \quad (6)$$

https://doi.org/10.1021/acsomega.1c00908
ACS Omega 2021, 6, 13124−13133

The details of the parametric description in eq 6 and the calculation process for η's are described in the Supporting Information.

The HER reaction progress is also investigated in an acidic environment, and the catalytic performance can be evaluated by calculating the Gibbs free energy ΔG_{H*} of adsorbed hydrogen, defined as[6]

$$\Delta G_{H*} = \Delta E_{H*} + \Delta ZPE - T\Delta S \tag{7}$$

where ΔZPE and ΔS are the zero-point energy change and vibrational entropy correction and ΔE_{H*} is the adsorbed energy of H* and can be calculated by[10]

$$\Delta E_{H*} = E_{H*} - E_{\text{surface}} - 1/2E_{H_2} \tag{8}$$

where E_{H*} and E_{surface} are the total energies of the surface with and without adsorbed H*, respectively, and E_{H_2} is the total energy of the gas-phase H_2 molecule. The vibrational entropy of H* is negligible; hence, $\Delta S = -1/2S_{H_2}$, where S_{H_2} is the entropy of H_2 in the gas phase under standard conditions, as shown in Table S1. Therefore, ΔG_{H*} with the overall correction can be written as[35]

$$\Delta G_{H*} = \Delta E_{H*} + 0.24 \text{ eV} \tag{9}$$

■ RESULTS AND DISCUSSION

The ORR (η^{ORR}) and OER (η^{OER}) overpotentials are usually used to characterize the ORR/OER catalytic performance, which can be obtained from the reaction free-energy diagrams.[33,34,36] Figure 1a,b displays the free-energy diagrams for the ORR/OER of pristine black arsenene (b-As) and gray arsenene (g-As) at different electrode potentials *U*. The forward ($2H_2O + * \rightarrow O_2$) and backward ($O_2 \rightarrow 2H_2O + *$) processes represent the OER and ORR, respectively. The overpotentials of η^{OER} and η^{ORR} are denoted by blue and red arrows, and the adsorbed intermediates (O*, OH*, and OOH*) are displayed below each free-energy diagram. For the OER on pristine b-As in Figure 1a, at $U = 1.23$ V of the equilibrium potential shown in green lines, the transformations of OH* → O* and OOH* → O_2 are downhill. However, elementary reaction steps of H_2O → OH* and O* → OOH* both are uphill, and the highest free-energy gain of 1.85 eV for O* → OOH* has to be overcome. Only when *U* increases to 3.08 V, as shown in blue lines, can all reaction steps become downhill and occur spontaneously. Hence, 1.85 V is the OER overpotential η^{OER} and the step of O* → OOH* is the rate-determining step (RDS). For the ORR process, at $U = 1.23$ V, the step of O_2 → OOH* possesses the highest free-energy gain of 2.49 eV, determining the ORR-RDS. As shown in the red lines, at $U = -1.26$ V, this free-energy gain will vanish and all steps are downhill, corresponding to $\eta^{ORR} = 2.49$ V. Similarly, for pristine g-As in Figure 1b, the RDSs of the OER and ORR also arise from O* → OOH* with $\eta^{OER} = 1.72$ V and from O_2 → OOH* with $\eta^{ORR} = 2.40$ V, respectively, which are mainly attributed to the weak adsorption of the intermediate OOH*. According to the Sabatier principle, the catalytic activities strongly depend on the adsorption strength of intermediates, which should be not too weak nor too strong for an effective catalyst.[37] Too weak adsorption will result in an inefficient reaction, while too strong adsorption of the intermediates will gradually terminate the reaction by blocking the catalytic active sites. The calculated high OER and ORR overpotentials in Figure 1 indicate that pristine b-As and g-As could not act as effective catalysts.

To improve the catalytic properties of b-As and g-As, we employ chemical modification by embedding a variety of heteroatoms including O, C, P, S, and Sb into the arsenene lattice. The calculated formation energies E_f's for different kinds of *X*-doped (*X* = O, C, P, S, and Sb) b-As and g-As are presented in Figure 2a. For each heteroatom, two types of configurations with a single dopant and double dopants are calculated. The more negative value of E_f corresponds to more stable doping configurations. As shown in Figure 2a, compared to other heteroatoms, O atom doping exhibits a relatively smaller E_f value whether for a single dopant and double dopants, indicating that it is more likely to be embedded into b-As and g-As lattices than other heteroatoms. Furthermore, E_f's of double O-doped b-As_O^2 and g-As_O^2 are smaller than those of single O-doped b-As_O^1 and g-As_O^1, which suggests that the interaction with each other between O atoms can further help stabilize defective configuration. In addition, other double atom-doped configurations also exhibit a negative E_f value, such as g-As_C^2, b-As_C^2, and b-As_P^2. Based on the above analysis, in the following discussion, we will focus on the catalytic properties for the ORR, OER, and HER on O-doped b-As and g-As and add other stable heteroatom-doped configurations for comparison. Figure 2b−e displays the atomic structures of respective single and double O-doped b-As (b-As_O^1 and b-As_O^2) and g-As (g-As_O^1 and g-As_O^2). To further identify the stability of heteroatom-doped arsenene, we perform the ab initio molecular dynamic simulations at a temperature of 300 K to examine the dynamic stability. Figure S2 shows the fluctuation of the total energy during the MD simulations and the corresponding snapshots for representative b-As_O^2, g-As_C^2, and g-As_O^1. Compared with the initial snapshots at 0 ps, all structures exhibit slight changes at room temperature, suggesting the high structural stability.

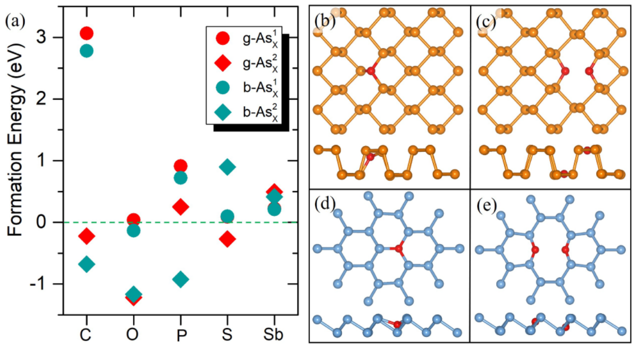

Figure 2. (a) Formation energy for single and double X-doped gray arsenene (g-As_X^1 and g-As_X^2) and black arsenene (b-As_X^1 and b-As_X^2) (*X* = C, O, P, S, and Sb). O-doped atomic structures of (b) g-As_O^1, (c) g-As_O^2, (d) b-As_O^1, and (e) b-As_O^2. Purple, blue, and red balls indicate As atoms in black and gray arsenene, and O atoms, respectively.

Figure 3a shows the calculated OER overpotentials η^{OER}'s at different active sites for pristine and O-doped b-As/g-As. For comparison, we add the overpotential data of C-doped b-As/g-As. Table 1 summarizes the calculated free energies of the adsorbed intermediates and overpotentials in investigated

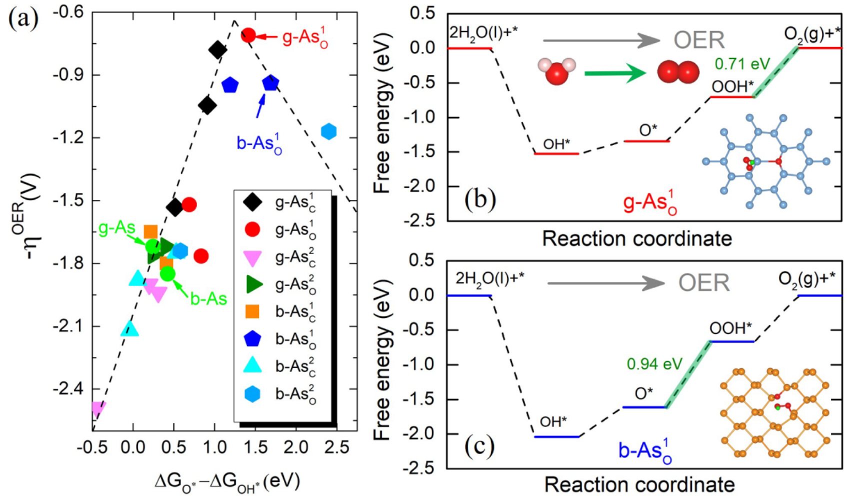

Figure 3. (a) Volcano plots for the OER vs the difference between adsorption energies of O* and OH* for single and double C- and O-doped b-As and g-As. Free-energy diagrams for the optimal OER on (b) g-As^1_O and (c) b-As^1_O at U = 1.23 V. The corresponding atomic structures of the adsorbed intermediate OOH* are shown in the insets.

Table 1. Adsorption Energies of Intermediates (O*, OH*, and OOH*) in Electronvolt, Reaction Free Energies in Electronvolt of Each Reactive Step along the OER Reaction Pathway and OER/ORR Overpotentials in Volt at Different Active sites for C- and O-doped black and gray arsenene[a]

		ΔG_{OH*}	ΔG_{O*}	ΔG_{OOH*}	ΔG_1	ΔG_2	ΔG_3	ΔG_4	η^{OER}	η^{ORR}
g-As^1_O	A	−0.30	1.11	2.97	−0.30	1.41	1.86	1.94	0.71	1.53
	B	0.95	1.64	4.38	0.95	0.69	2.74	0.54	1.52	0.68
	C	0.75	1.59	1.92	0.75	0.83	0.33	2.99	1.76	0.89
g-As^2_O	A	0.74	1.15	4.10	0.74	0.40	2.95	0.81	1.72	0.82
	B	1.19	1.44	4.44	1.19	0.25	2.99	0.47	1.76	0.97
b-As^1_O	A	−0.81	0.87	2.74	−0.81	1.68	1.86	2.17	0.94	2.04
	B	−0.01	1.18	3.36	−0.01	1.19	2.18	1.56	0.95	1.24
b-As^2_O	A	0.33	2.74	3.96	0.33	2.40	1.22	0.95	1.17	0.89
	B	0.64	1.22	4.19	0.64	0.58	2.97	0.72	1.74	0.65
g-As^1_C	A	0.43	1.48	3.50	0.43	1.04	2.00	1.42	0.78	0.79
	B	1.14	1.66	4.42	1.14	0.51	2.76	0.49	1.53	0.73
	C	0.62	1.54	3.84	0.62	0.91	2.27	1.10	1.04	0.60
g-As^2_C	A	1.98	1.54	5.26	1.98	−0.44	3.72	−0.34	2.49	1.67
	B	1.38	1.69	4.86	1.38	0.31	3.17	0.06	1.94	1.17
	C	1.68	1.87	5.00	1.68	0.20	3.13	−0.08	1.90	1.31
b-As^1_C	A	−0.06	0.16	3.04	−0.06	0.22	2.88	1.88	1.65	1.29
	B	0.84	1.25	4.29	0.84	0.41	3.03	0.62	1.80	0.81
b-As^2_C	A	1.72	1.78	4.89	1.72	0.06	3.11	0.03	1.88	1.20
	B	1.50	1.47	4.82	1.50	−0.04	3.35	0.10	2.12	1.27
	C	0.77	1.30	4.29	0.77	0.53	2.98	0.62	1.75	0.69

[a] The detailed atomic structures are displayed in Figure S3.

configurations, and atomic structures of O- and C-doped clusters with detailed active sites are shown in Figure S3. As shown in Figure 3a, the η^{OER}'s of these structures exhibit a typical volcano shape, suggesting that introducing heteroatoms can tune the OER catalytic activity in a wide range. Obviously, pristine b-As and g-As with high η^{OER} values of 1.85 and 1.72 V locate at the bottom of the OER volcano, indicating the poor OER catalytic activity. In contrast, close to the peak of the volcano, as shown by the red arrow, single O-doped g-As^1_O exhibits the lowest η^{OER} of 0.71 V, indicating improved OER catalytic activity. For O-doped b-As, the optimal OER catalytic active site also locates on the single O-doped configuration b-As^1_O with η^{OER} = 0.94 V, as denoted by the blue arrow. In addition, it is worth noting that single C-doped g-As^1_C shown by the black diamond also locates near the peak of the volcano, indicating excellent catalytic performance, but it is very difficult to prepare g-As^1_C in experiments because of its high E_f, as shown in Figure 2a. Therefore, we do not choose g-As^1_C as an effective OER catalyst.

The origin of reactive overpotentials can be better understood by plotting the free-energy diagrams, and the overpotentials strongly depend on the free-energy difference

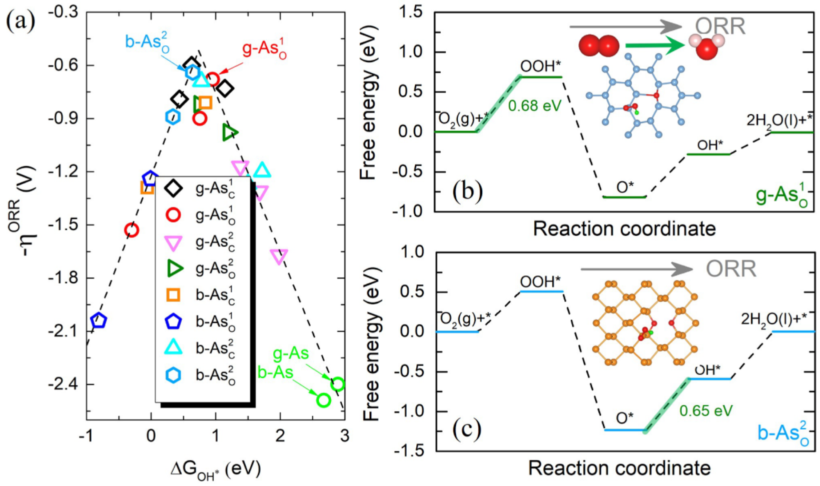

Figure 4. (a) Volcano plots for the ORR vs adsorption energies of OH* on single and double C and O-doped b-As and g-As. Free-energy diagrams for the optimal ORR on (b) g-As$_\text{O}^1$ and (c) b-As$_\text{O}^2$ at U = 1.23 V. The corresponding atomic structures of the adsorbed intermediate OOH* are shown in the insets.

between two reactive intermediates of the RDSs. Figure 3b,c shows the OER free-energy diagrams on g-As$_\text{O}^1$ and b-As$_\text{O}^1$ at the equilibrium potential (U = 1.23 V), respectively. By comparing the free-energy diagrams at U = 1.23 V in Figures 1a,b and 3b,c, it is clearly shown that the introduction of O atoms considerably tunes and enhances the binding strength of reactive intermediates (O*, OH*, and OOH*) with more negative adsorption energies. For the OER on g-As$_\text{O}^1$ in Figure 3b, the RDS has translated to the step of OOH* → O_2 (g) with a free-energy difference of 0.71 eV, corresponding to the η^{OER} of 0.71 V. For b-As$_\text{O}$ in Figure 3c, compared with pristine b-As in Figure 1b, the step of O* → OOH* is still the OER RDS, while the free-energy gain has been reduced to 0.94 eV, determining a better η^{OER} = 0.94 V.

Similarly, in Figure 4a, we summarize the ORR overpotentials η^{ORR}'s at different active sites on pristine and C- and O-doped b-As/g-As. ORR overpotentials exhibit a similar volcano shape and can be tuned within a wide range. Clearly, as denoted by the green circles, pristine b-As and g-As locate at the bottom of the volcano shape, indicating poor catalytic activity. For b-As, double O-doped b-As$_\text{O}^2$ locates near the top of the volcano peak and exhibits the best ORR catalytic performance, with the lowest η^{ORR} = 0.65 V. Among all O-doped g-As, g-As$_\text{O}^1$ is the most effective ORR catalytic structure, with η^{ORR} = 0.68 V. The corresponding ORR free-energy diagrams on g-As$_\text{O}^1$ and b-As$_\text{O}^2$ are shown in Figure 4b,c, respectively. The free-energy diagrams in Figure 1 have shown that the step of O_2 → OOH* determines the ORR RDS of pristine structures. In Figure 4b, the ORR RDS of g-As$_\text{O}^1$ still originates from O_2 → OOH*, but compared to over-high η^{ORR} of 2.40 V on pristine g-As, the η^{ORR} has been significantly reduced to 0.68 V due to the enhanced adsorption of OOH*. For b-As$_\text{O}^2$ in Figure 4c, the ORR RDS has translated to the step of O → OH*, and excessive overpotential for pristine b-As (2.49 V) has been optimized to 0.65 V.

The improved OER/ORR activities of the above-mentioned O-doped configurations can be effectively attributed to the redistribution of surface charges induced by the introduction of O dopants into g- and b-As lattices. As shown in Figure S5, the distribution map of the charge density difference clearly demonstrates strong charge transfer between O atoms and the surrounding As atoms. Furthermore, Bader charge analysis shows that due to the larger electronegativity of O than As, the embedded O atoms attract more electrons with a negative Bader charge value, while the surrounding As atoms lose electrons and become positively charged. These As atoms with positive effective charges will facilitate the adsorption of reactive intermediates (O*, OH*, and OOH*) with negative charges and can act as potential active sites. As shown in Figure S6, the adsorbed intermediates usually obtain electrons from the catalyst surface and compared with the adsorption on the pristine surface, there is much more charge transfer from the O-doped surface to intermediates. Therefore, the resulting charge transfer has an effect on the ability of the adsorbed intermediates to obtain electrons from the catalyst surface, which is related to the adsorption strength of the intermediates, thus tuning the catalytic activity within a wide range.

Nowadays, people are developing high-performance bifunctional catalysts, which can catalyze the ORR and OER simultaneously.[1,38] The bifunctional catalytic performance could be well evaluated by calculating the ORR/OER potential gap, that is, the sum of η^{ORR} and η^{OER}.[39,40] The lower ORR/OER potential gap corresponds to a better bifunctional catalytic activity. Figure 3a shows that g-As$_\text{O}^1$ exhibits the best OER catalytic performance, with η^{OER} = 0.71 V. Considering that the optimal ORR activity with η^{ORR} = 0.68 V, as shown in Figure 4a, g-As$_\text{O}^1$ shows great potential to act as an effective bifunctional catalyst with a low ORR/OER potential gap of 1.39 V.

To better understand the overpotential origin, Figure 5a,b displays more detailed free-energy diagrams for the optimal OER on g-As$_\text{O}^1$ and ORR on b-As$_\text{O}^2$ at different electrode potentials, respectively. In Figure 5a, for the OER on g-As$_\text{O}^1$, when the electrode potential U is 0 V, only the step of H_2O → OH* is downhill and other steps of OH* → O*, O* → OOH*, and OOH* → O_2 are uphill. As shown by the green lines, when U increases to the equilibrium potential 1.23 V, the

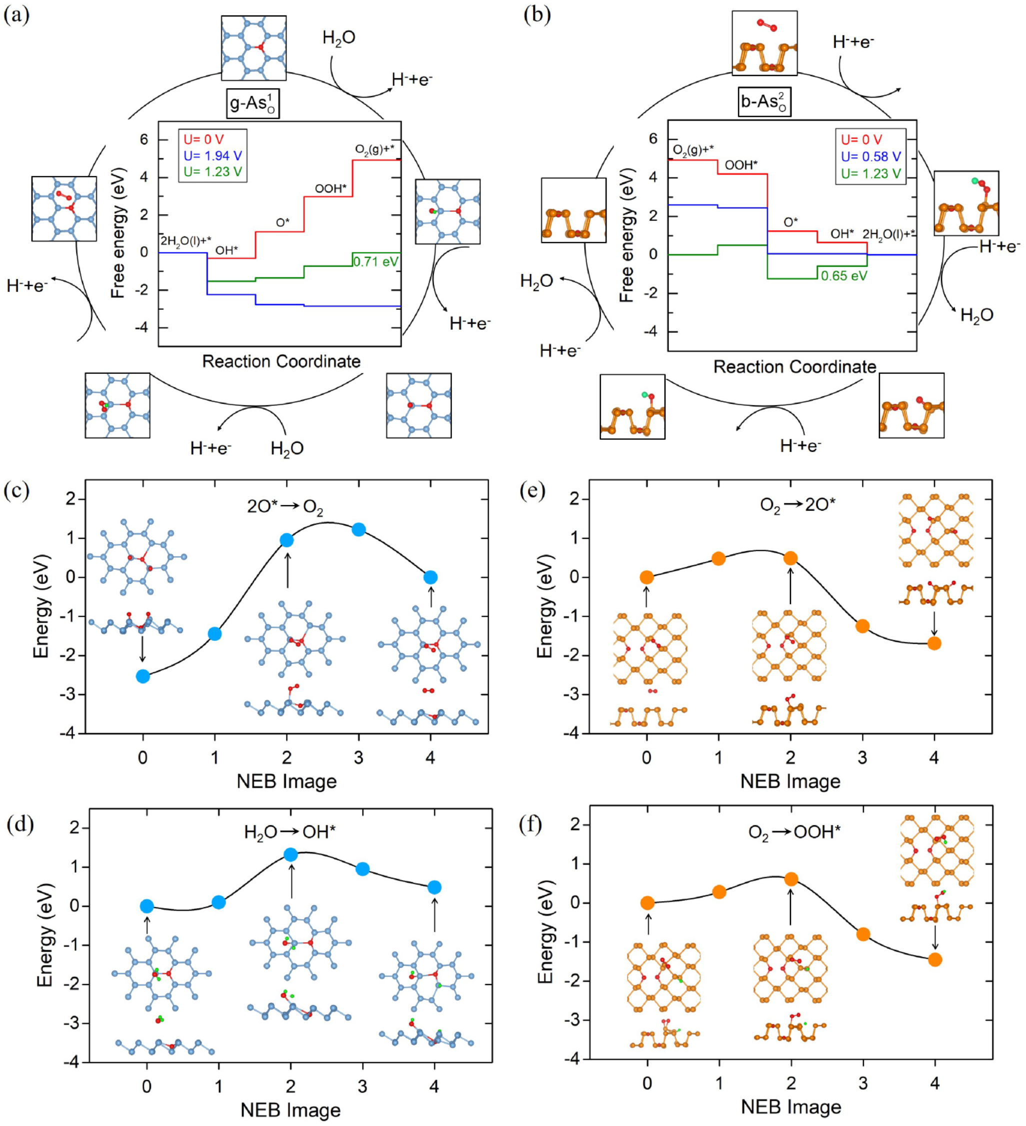

Figure 5. Free-energy diagrams for the optimal (a) OER on g-As^1_O and (b) ORR on b-As^2_O at different electrode potentials U. The adsorbed intermediates O*, OH*, and OOH* on g-As^1_O and b-As^2_O are also shown. The kinetic barriers for (c) 2O* → O_2 and (d) H_2O → OH* on g-As^1_O, and (e) O_2 dissociation via O_2 → 2O* and (f) O_2 → OOH* on b-As^2_O.

free-energy gains for the steps OH* → O*, O* → OOH*, and OOH* → O_2 have to be greatly reduced, but these three reactive steps are still uphill, with the highest free-energy gain of 0.71 eV for OOH* → O_2. Only when U increases to 1.94 V shown by the blue lines, the free-energy gain of OOH* → O_2 could be reduced to zero and all reactive steps become downhill, indicating that the OER reaction can occur spontaneously. Therefore, η^{OER} is 1.94−1.23 = 0.71 V and the RDS is the transformation from OOH* to O_2. For the ORR on b-As^2_O in Figure 5b, at U = 0 V, all steps are downhill. However, when U increases to the equilibrium potential 1.23 V, three uphill steps appear and the transformation from O* to OH* of the most endoergic step possesses the highest free-energy gain of 0.65 eV. This free-energy gain will be reduced to zero only when U decreases to 0.58 V, corresponding to the ORR RDS of O* → OH*, with η^{ORR} of 1.23−0.58 = 0.65 V. In addition, adsorbed intermediates O*, OH*, and OOH* on g-As^1_O and b-As^2_O are shown in each diagram. The detailed top and side views of atomic structures and charge density difference of the adsorbed intermediates are displayed in Figure S6. It is clearly shown that the reactive active sites in g-As^1_O and b-As^2_O locate at As sites around embedded O atoms, and strong charge transfer usually occur at adsorbed intermediates, active sites, and neighboring As atoms.

Through evaluating the kinetic barrier using the climbing image nudged elastic band method,[32,41] we further examine the possibility of particular reactive steps, in which two adsorbed O* species combine to form a O_2 molecule (2O* → O_2) on g-As^1_O for the OER and a O_2 molecule dissociates to two O* species (O_2 → 2O*) on b-As^2_O for the ORR. For comparison, we also examine the kinetic feasibility of the OER and ORR initial reaction steps of H_2O → OH* on g-As^1_O and O_2 → OOH* on b-As^2_O, as shown in Figure 5d,f, respectively. Figure 5c shows the reaction progress of 2O* → O_2 on g-As^1_O, and it is shown that the progress is endothermic with a high energy

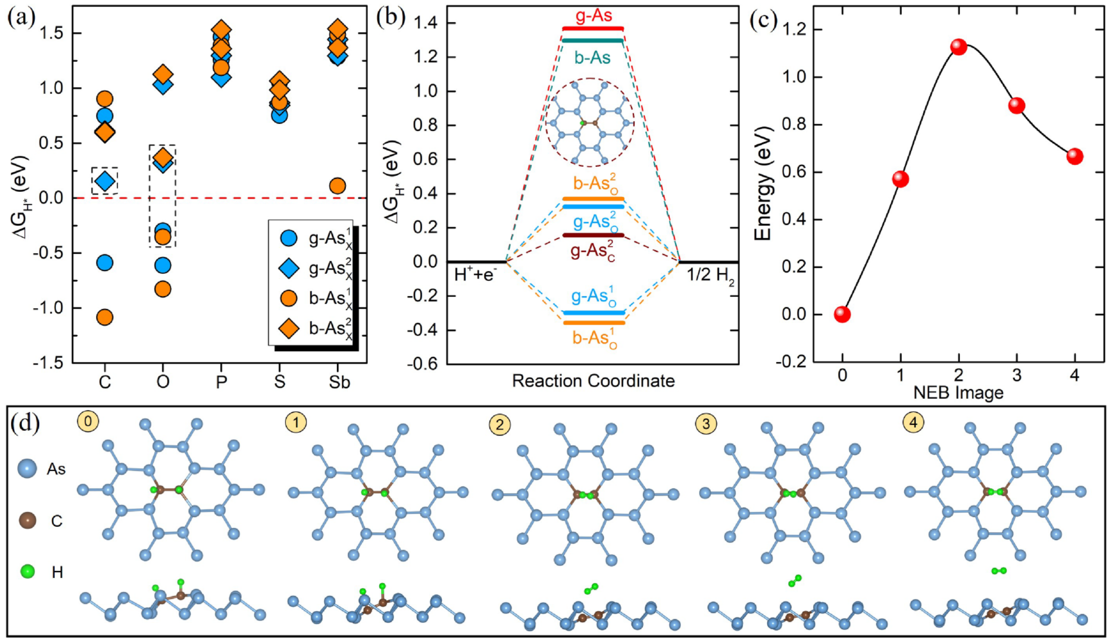

Figure 6. (a) Calculated ΔG_{H*} for single- and double-doped structures (g-As^1_X, g-As^2_X, b-As^1_X and b-As^2_X, X = C, O, P, S, and Sb). (b) HER free-energy diagrams for b-As, g-As, g-As^1_O, g-As^1_O, g-As^2_O, b-As^1_O, and b-As^2_O. (c) Kinetic barriers of the HER Tafel-step reaction on g-As^1_C. (d) Atomic structures of initial, final, and intermediate NEB images.

barrier of ∼3.7 eV. This indicates that during the OER on g-As^1_O, O* species cannot directly coalesce to produce O_2 but must be assisted by the OOH* intermediate group, as shown in Figure 5a. In contrast, in Figure 5d, the initial step of H_2O → OH* on g-As^1_O exhibits a lower energy barrier of ∼1.32 eV, suggesting better OER kinetic feasibility. In Figure 5e, the energy barrier for the dissociative O_2 → 2O* pathway on b-As^2_O is as low as ∼0.48 eV with the exothermic feature, indicating that this reaction pathway could easily occur kinetically. In addition, from Figure 5f, it can be seen that the associative reaction step of O_2 → OOH* on b-As^2_O also possesses a low barrier of ∼0.61 eV, and the exothermic feature indicates that this pathway is favored energetically. Therefore, for the ORR on b-As^2_O, the O_2 molecule may be able to efficiently dissociate through dual reaction pathways: one is the step-by-step reaction accompanied by the formation of the OOH* intermediate (O_2 → OOH* → 2O*), or the O_2 molecule dissociates directly into O* (O_2 → 2O*). Such dual reaction pathways will promote the ORR reaction rate on b-As^2_O.

Furthermore, the influence of doping elements on HER catalytic activity is also investigated. The HER catalytic performance can be well characterized by the Gibbs free energy of H* adsorption (ΔG_{H*}) on the reactive surface.[42,43] The value of ΔG_{H*} for an ideal catalyst should be close to zero ($\Delta G_{H*} \sim 0$). High ΔG_{H*} will lead to weak hydrogen adsorption on the catalyst surface, while low ΔG_{H*} represents the strong binding of adsorbed hydrogen and the surface, which will go against the dissociation of the generated H_2 molecule, both resulting in a slow HER reaction. For better comparing the ΔG_{H*} between different doping systems, we summarize the calculated ΔG_{H*} at different reactive sites on g-As^1_X, g-As^2_X, b-As^1_X, and b-As^2_X in Figure 6a. It can be seen that embedded heteroatoms can tune ΔG_{H*} within a wide range, especially for C and O dopants. Among these doped configurations, g-As^2_C, g-As^1_O, g-As^2_O, b-As^1_O, b-As^2_O, and b-As$^1_{Sb}$ can optimize ΔG_{H*} to an appropriate value, which is close to zero and eligible for HER catalysis, indicating improved reaction activity. Considering the high formation energy of Sb dopants in Figure 2a, we only select C- and O-doped configurations as effective HER catalysts, as labeled by black dotted rectangles in Figure 6a. Figure 6b shows the HER free-energy diagrams for pristine b-As/g-As, g-As^2_C, g-As^1_O, g-As^2_O, b-As^1_O, and b-As^2_O. As indicated by green and red lines, pristine b-As and g-As exhibit very weak hydrogen adsorption, with ΔG_{H*} = 1.29 and 1.38 eV, which are not conducive to the catalytic reaction and even prevents the reaction from occurring. Clearly, embedding C and O dopants can provide sufficient adsorption strength, especially for g-As^2_C with ΔG_{H*} = 0.15 eV. The atomic structure of g-As^2_C with adsorbed H* is displayed in the inset of Figure 6b and the active site arises from the embedded C atom. In Figure S5, the charge density difference and Bader charge analysis clearly indicate that the enhanced HER activity mainly arises from the strong charge transfer induced by the embedded O and C dopants, which can effectively improve the adsorption strength of H*.

For reducing protons to hydrogen in acid media, there exist two different types of reaction pathways of the Volmer−Tafel and Volmer−Heyrovsky mechanism.[6] The Volmer reaction is the first step in the HER process and refers to forming adsorbed H* from the initial adsorption of proton in acid solution. Based on the Volmer reaction, in the Volmer−Tafel mechanism, two adjacent adsorbed H* species then react to form a H_2 molecule (H* + H* → H_2). However, in the Volmer−Heyrovsky mechanism, adsorbed H* species reacts with a proton accompanied by one electron to form a H_2 molecule (H* + H^+ + e^- → H_2). Figure 6c presents the kinetic progress of the HER on optimal g-As_C^2 via the Tafel-step reaction. The kinetic barrier for this reaction is as high as ∼1.13 eV, comparable to that of graphene(G)/MXene heterostructures (1.56 and 1.33 eV for G/Mo_2C and G/V_2C, respectively)[44] and MoS_2 edges (1.0−1.5 eV),[6] which will severely slow down the Tafel reaction. However, the Heyrovsky-step reaction with a lower kinetic barrier is usually much faster than the Tafel-step reaction.[6] Therefore, the Volmer−Heyrovsky mechanism may be the main reaction pathway of the HER on g-As_C^1.

Since the electrocatalytic processes typically take place at the solid−liquid interfaces,[45] it is very necessary to explore the influence of the solvent effect on catalytic activities. As shown in Figures S7−S9, we adopted the simple explicit model to tackle solvent effects, in which multiple water molecules are added on the catalyst surfaces to model the aqueous interface. The atomic structures of intermediates clearly indicate that there exists obvious hydrogen bonding between adsorbates and water molecules, which could further stabilize the adsorption of intermediates. As shown in Figures S7 and S8, the hydrogen bonding has different stabilizing effects for intermediates O*, OH*, and OOH* on g-As_O^1 and b-As_O^2, affecting the catalytic performance to some extent. For example, the calculated OER overpotential on g-As_O^1 degenerates from 0.71 to 0.80 V at an aqueous interface. For the HER process in Figure S9, it is clearly seen that the H* adsorption on g-As_C^2 is further stabilized by hydrogen bonding with a lower ΔG_{H*} value; hence, the solvent effects give rise to a positive influence for the HER activity on g-As_C^2. Therefore, to more accurately describe the catalytic characteristics of real solid−liquid systems, solvent effects should be carefully considered in computational simulation.

As we know that electrical conductivity is a critical characteristic quantity that determines the electron-transfer efficiency and catalytic activity, which requires that the catalysts should be metallic or semiconductors. Therefore, it is very necessary to characterize the electrical conductivity properties of catalysts. Figure S10 shows the density of states of g-As_O^1, b-As_O^2, and g-As_C^2 with optimal catalytic activities. It can be clearly seen that b-As_O^2 and g-As_C^2 demonstrate obvious semiconductor properties, and g-As_O^1 exhibits favorable metallicity, which indicates that these explored surfaces possess good electrical conductivity and can guarantee efficient electron transfer during catalytic reaction progress. The calculated optimal overpotentials/ΔG_{H*} and good electron-transfer characteristics together prove the feasibility of our proposed effective catalysts.

■ CONCLUSIONS

In summary, using DFT calculations, we study the ORR, OER, and HER catalytic activities of pristine and various heteroatom (O, C, P, S, and Sb)-doped b-As/g-As. The results show that pristine b-As and g-As exhibit poor catalytic performance for the ORR, OER, and HER. Embedding heteroatoms can effectively tune the adsorption strength of reactive intermediations and thus improve catalytic activities. Compared with other candidate dopants (C, P, S, and Sb), O atoms are more likely to be embedded into b-As and g-As lattices. More importantly, O atom-modified b-As and g-As show superior catalytic properties for the OER and ORR. For g-As, the OER and ORR catalytic activity can be optimized simultaneously on single g-As_O^1, which exhibits great potential as effective bifunctional catalysts. However, the optimal OER and ORR catalytic performance on b-As can be realized in b-As_O^1 and b-As_O^2, respectively. NEB calculations suggest that b-As_O^2 can achieve the dual ORR reaction pathway through O_2 → OOH* → 2O* and O_2 → 2O*. For the HER, C-doped g-As_C^2 shows the best catalytic performance, with an appropriate ΔG_{H*} of 0.15 eV, and the Volmer−Heyrovsky mechanism is the main reaction pathway. These findings would trigger more theoretical and experimental works to further investigate the catalytic properties of As-based materials.

■ ASSOCIATED CONTENT

Supporting Information

The Supporting Information is available free of charge at https://pubs.acs.org/doi/10.1021/acsomega.1c00908.

Further computational setups, detailed atomic structures of pristine black/gray arsenene and C- and O-doped configurations; scaling relationship between the adsorbed energies of reactive intermediates; and charge density difference for O*, OH*, and OOH* on g-As_O^1 and b-As_O^2 (PDF)

■ AUTHOR INFORMATION

Corresponding Authors

Xiong-Xiong Xue − *School of Physics and Optoelectronics, Xiangtan University, Xiangtan 411105, China*; orcid.org/0000-0003-2342-1003; Email: xxxue@hnu.edu.cn

Yexin Feng − *Hunan Provincial Key Laboratory of Low-Dimensional Structural Physics & Devices, School of Physics and Electronics, Hunan University, Changsha 410082, China*; Email: yexinfeng@hnu.edu.cn

Authors

Sengpajan Santisouk − *Hunan Provincial Key Laboratory of Low-Dimensional Structural Physics & Devices, School of Physics and Electronics, Hunan University, Changsha 410082, China*

Phoxay Sengdala − *Hunan Provincial Key Laboratory of Low-Dimensional Structural Physics & Devices, School of Physics and Electronics, Hunan University, Changsha 410082, China*

Xingxing Jiang − *Hunan Provincial Key Laboratory of Low-Dimensional Structural Physics & Devices, School of Physics and Electronics, Hunan University, Changsha 410082, China*; orcid.org/0000-0001-8815-3914

Ke-Qiu Chen − *Hunan Provincial Key Laboratory of Low-Dimensional Structural Physics & Devices, School of Physics and Electronics, Hunan University, Changsha 410082, China*; orcid.org/0000-0001-8627-0498

Complete contact information is available at: https://pubs.acs.org/10.1021/acsomega.1c00908

Author Contributions

#S.S. and P.S. contributed equally to this work.

Notes

The authors declare no competing financial interest.

■ ACKNOWLEDGMENTS

Y.F. is supported by the National Science Foundation of China (grant nos. 11604092 and 11634001) and the National Basic Research Programs of China (grant no. 2016YFA0300900). The computational resources were provided by the supercomputer TianHe-1 in Changsha, China.

■ REFERENCES

(1) Zhang, J.; Zhao, Z.; Xia, Z.; Dai, L. A Metal-Free Bifunctional Electrocatalyst for Oxygen Reduction and Oxygen Evolution Reactions. *Nat. Nanotechnol.* **2015**, *10*, 444−452.

(2) Xue, X. X.; Tang, L. M.; Chen, K.; Zhang, L.; Wang, E. G.; Feng, Y. Bifunctional Mechanism of N, P Co-Doped Graphene for Catalyzing Oxygen Reduction and Evolution Reactions. *J. Chem. Phys.* **2019**, *150*, No. 104701.

(3) Ren, X.; Zhou, J.; Qi, X.; Liu, Y.; Huang, Z.; Li, Z.; Ge, Y.; Dhanabalan, S. C.; Ponraj, J. S.; Wang, S.; Zhong, J.; Zhang, H. Few-Layer Black Phosphorus Nanosheets as Electrocatalysts for Highly Efficient Oxygen Evolution Reaction. *Adv. Energy Mater.* **2017**, *7*, No. 1700396.

(4) Xue, X.-X.; Shen, S.; Jiang, X.; Sengdala, P.; Chen, K.; Feng, Y. Tuning the Catalytic Property of Phosphorene for Oxygen Evolution and Reduction Reactions by Changing Oxidation Degree. *J. Phys. Chem. Lett.* **2019**, *10*, 3440−3446.

(5) Zhu, J.; Jiang, X.; Yang, Y.; Chen, Q.; Xue, X. X.; Chen, K.; Feng, Y. Synergy of Tellurium and Defects in Control of Activity of Phosphorene for Oxygen Evolution and Reduction Reactions. *Phys. Chem. Chem. Phys.* **2019**, *21*, 22939−22946.

(6) Tang, Q.; Jiang, D.-E. Mechanism of Hydrogen Evolution Reaction on 1T-MoS_2 from First Principles. *ACS Catal.* **2016**, *6*, 4953−4961.

(7) Shao, G.; Xue, X. X.; Wu, B.; Lin, Y. C.; Ouzounian, M.; Hu, T. S.; Xu, Y.; Liu, X.; Li, S.; Suenaga, K.; Feng, Y.; Liu, S. Template-Assisted Synthesis of Metallic 1T'-$Sn_{0.3}W_{0.7}S_2$ Nanosheets for Hydrogen Evolution Reaction. *Adv. Funct. Mater.* **2019**, *30*, No. 1906069.

(8) Zhang, X.; Chen, A.; Zhang, Z.; Jiao, M.; Zhou, Z. Transition Metal Anchored C_2N Monolayers as Efficient Bifunctional Electrocatalysts for Hydrogen and Oxygen Evolution Reactions. *J. Mater. Chem. A* **2018**, *6*, 11446−11452.

(9) Gao, G.; Waclawik, E. R.; Du, A. Computational Screening of Two-Dimensional Coordination Polymers as Efficient Catalysts for Oxygen Evolution and Reduction Reaction. *J. Catal.* **2017**, *352*, 579−585.

(10) Gao, G.; O'Mullane, A. P.; Du, A. 2d Mxenes: A New Family of Promising Catalysts for the Hydrogen Evolution Reaction. *ACS Catal.* **2017**, *7*, 494−500.

(11) Kou, L.; Ma, Y.; Tan, X.; Frauenheim, T.; Du, A.; Smith, S. Structural and Electronic Properties of Layered Arsenic and Antimony Arsenide. *J. Phys. Chem. C* **2015**, *119*, 6918−6922.

(12) Ersan, F.; Aktürk, E.; Ciraci, S. Interaction of Adatoms and Molecules with Single-Layer Arsenene Phases. *J. Phys. Chem. C* **2016**, *120*, 14345−14355.

(13) Zhang, S.; Xie, M.; Li, F.; Yan, Z.; Li, Y.; Kan, E.; Liu, W.; Chen, Z.; Zeng, H. Semiconducting Group 15 Monolayers: A Broad Range of Band Gaps and High Carrier Mobilities. *Angew. Chem.* **2016**, *128*, 1698−1701.

(14) Kamal, C.; Ezawa, M. Arsenene: Two-Dimensional Buckled and Puckered Honeycomb Arsenic Systems. *Phys. Rev. B* **2015**, *91*, 085423.

(15) Chen, Y.; Chen, C.; Kealhofer, R.; Liu, H.; Yuan, Z.; Jiang, L.; Suh, J.; Park, J.; Ko, C.; Choe, H. S.; Avila, J.; Zhong, M.; Wei, Z.; Li, J.; Gao, H.; Liu, Y.; Analytis, J.; Xia, Q.; Asensio, M. C.; Wu, J. Black Arsenic: A Layered Semiconductor with Extreme in-Plane Anisotropy. *Adv. Mater.* **2018**, *30*, No. e1800754.

(16) Zhong, M.; Xia, Q.; Pan, L.; Liu, Y.; Chen, Y.; Deng, H.-X.; Li, J.; Wei, Z. Thickness-Dependent Carrier Transport Characteristics of a New 2d Elemental Semiconductor: Black Arsenic. *Adv. Funct. Mater.* **2018**, *28*, No. 1802581.

(17) Luo, K.; Chen, S.; Duan, C. Indirect-Direct Band Gap Transition of Two-Dimensional Arsenic Layered Semiconductors—Cousins of Black Phosphorus. *Sci. China: Phys., Mech. Astron.* **2015**, *58*, No. 87301.

(18) Zhang, S.; Yan, Z.; Li, Y.; Chen, Z.; Zeng, H. Atomically Thin Arsenene and Antimonene: Semimetal-Semiconductor and Indirect-Direct Band-Gap Transitions. *Angew. Chem., Int. Ed. Engl.* **2015**, *54*, 3112−3115.

(19) Zhang, Z.; Xie, J.; Yang, D.; Wang, Y.; Si, M.; Xue, D. Manifestation of Unexpected Semiconducting Properties in Few-Layer Orthorhombic Arsenene. *Appl. Phys. Express* **2015**, *8*, No. 055201.

(20) Sun, Y.; Wang, D.; Shuai, Z. Puckered Arsenene: A Promising Room-Temperature Thermoelectric Material from First-Principles Prediction. *J. Phys. Chem. C* **2017**, *121*, 19080−19086.

(21) Zeraati, M.; Vaez Allaei, S. M.; Abdolhosseini Sarsari, I.; Pourfath, M.; Donadio, D. Highly Anisotropic Thermal Conductivity of Arsenene: An Ab Initio Study. *Phys. Rev. B* **2016**, *93*, No. 085424.

(22) Sturala, J.; Ambrosi, A.; Sofer, Z.; Pumera, M. Covalent Functionalization of Exfoliated Arsenic with Chlorocarbene. *Angew. Chem., Int. Ed. Engl.* **2018**, *57*, 14837−14840.

(23) Li, Z.; Xu, W.; Yu, Y.; Du, H.; Zhen, K.; Wang, J.; Luo, L.; Qiu, H.; Yang, X. Monolayer Hexagonal Arsenene with Tunable Electronic Structures and Magnetic Properties Via Impurity Doping. *J. Mater. Chem. C* **2016**, *4*, 362−370.

(24) Shen, S.; Gan, Y.; Xue, X.-X.; Wei, J.; Tang, L.-M.; Chen, K.; Feng, Y. Role of Defects on the Catalytic Property of 2D Black Arsenic for Hydrogen Evolution Reaction. *Appl. Phys. Express* **2019**, *12*, No. 075502.

(25) Kresse, G.; Furthmüller, J. Efficiency of Ab-Initio Total Energy Calculations for Metals and Semiconductors Using a Plane-Wave Basis Set. *Comput. Mater. Sci.* **1996**, *6*, 15−50.

(26) Kresse, G.; Furthmüller, J. Efficient Iterative Schemes for Ab Initio Total-Energy Calculations Using a Plane-Wave Basis Set. *Phys. Rev. B* **1996**, *54*, No. 11169.

(27) Kresse, G.; Joubert, D. From Ultrasoft Pseudopotentials to the Projector Augmented-Wave Method. *Phys. Rev. B* **1999**, *59*, No. 1758.

(28) Perdew, J. P.; Burke, K.; Ernzerhof, M. Generalized Gradient Approximation Made Simple. *Phys. Rev. Lett.* **1996**, *77*, 3865.

(29) Xue, X. X.; Feng, Y. X.; Liao, L.; Chen, Q. J.; Wang, D.; Tang, L. M.; Chen, K. Strain Tuning of Electronic Properties of Various Dimension Elemental Tellurium with Broken Screw Symmetry. *J. Phys.: Condens. Matter* **2018**, *30*, No. 125001.

(30) Grimme, S.; Antony, J.; Ehrlich, S.; Krieg, H. A Consistent and Accurate Ab Initio Parametrization of Density Functional Dispersion Correction (DFT-D) for the 94 Elements H-Pu. *J. Chem. Phys.* **2010**, *132*, No. 154104.

(31) Feng, Y.; Chen, K.; Li, X. Z.; Wang, E.; Zhang, L. Hydrogen Induced Contrasting Modes of Initial Nucleations of Graphene on Transition Metal Surfaces. *J. Chem. Phys.* **2017**, *146*, No. 034704.

(32) Xue, X. X.; Feng, Y.; Chen, K.; Zhang, L. The Vertical Growth of MoS_2 Layers at the Initial Stage of CVD from First-Principles. *J. Chem. Phys.* **2018**, *148*, No. 134704.

(33) Nørskov, J. K.; Rossmeisl, J.; Logadottir, A.; Lindqvist, L.; Kitchin, J. R.; Bligaard, T.; Jonsson, H. Origin of the Overpotential for Oxygen Reduction at a Fuel-Cell Cathode. *J. Phys. Chem. B* **2004**, *108*, 17886−17892.

(34) Man, I. C.; Su, H.-Y.; Calle-Vallejo, F.; Hansen, H. A.; Martínez, J. I.; Inoglu, N. G.; Kitchin, J.; Jaramillo, T. F.; Nørskov, J. K.; Rossmeisl, J. Universality in Oxygen Evolution Electrocatalysis on Oxide Surfaces. *ChemCatChem* **2011**, *3*, 1159−1165.

(35) Noerskov, J. K.; Bligaard, T.; Logadottir, A.; Kitchin, J. R.; Chen, J. G.; Pandelov, S.; Stimming, U.; Trends in the Exchange Current for Hydrogen Evolution. *J. Electrochem. Soc.* **2005**, *36*, J23.

(36) Hajiyani, H.; Pentcheva, R. Influence of 3d, 4d, and 5d Dopants on the Oxygen Evolution Reaction at Alpha-Fe_2O_3(0001) under Dark and Illumination Conditions. *J. Chem. Phys.* **2020**, *152*, No. 124709.

(37) Sabatier, P. Hydrogénations et déshydrogénations par catalyse. *Eur. J. Inorg. Chem.* **1911**, *44*, 1984−2001.

(38) Li, R.; Wei, Z.; Gou, X. Nitrogen and Phosphorus Dual-Doped Graphene/Carbon Nanosheets as Bifunctional Electrocatalysts for Oxygen Reduction and Evolution. *ACS Catal.* **2015**, *5*, 4133−4142.

(39) Gorlin, Y.; Jaramillo, T. F. A Bifunctional Nonprecious Metal Catalyst for Oxygen Reduction and Water Oxidation. *J. Am. Chem. Soc.* **2010**, *132*, 13612−13614.

(40) Tang, C.; Wang, H. F.; Chen, X.; Li, B. Q.; Hou, T. Z.; Zhang, B.; Zhang, Q.; Titirici, M. M.; Wei, F. Topological Defects in Metal-Free Nanocarbon for Oxygen Electrocatalysis. *Adv. Mater.* **2016**, *28*, 6845−6851.

(41) Henkelman, G.; Uberuaga, B. P.; Jónsson, H. A Climbing Image Nudged Elastic Band Method for Finding Saddle Points and Minimum Energy Paths. *J. Chem. Phys.* **2000**, *113*, 9901−9904.

(42) Greeley, J.; Jaramillo, T. F.; Bonde, J.; Chorkendorff, I. B.; Norskov, J. K. Computational High-Throughput Screening of Electrocatalytic Materials for Hydrogen Evolution. *Nat. Mater.* **2006**, *5*, 909−913.

(43) Jiao, Y.; Zheng, Y.; Davey, K.; Qiao, S.-Z. Activity Origin and Catalyst Design Principles For electrocatalytic Hydrogen Evolution on Heteroatom-Doped graphene. *Nat. Energy* **2016**, *1*, No. 16130.

(44) Zhou, S.; Yang, X.; Pei, W.; Liu, N.; Zhao, J. Heterostructures of Mxenes and N-Doped Graphene as Highly Active Bifunctional Electrocatalysts. *Nanoscale* **2018**, *10*, 10876−10883.

(45) Zhang, X.; Chen, A.; Chen, L.; Zhou, Z. 2D Materials Bridging Experiments and Computations for Electro/Photocatalysis. *Adv. Energy Mater.* **2021**, No. 2003841.